Mechanism and Machine Theory 164 (2021) 104408

Contents lists available at ScienceDirect

Mechanism and Machine Theory

journal homepage: www.elsevier.com/locate/mechmachtheory

Research paper

Computerized generation and tooth contact analysis of spherical gear couplings for high misalignment applications

Aurea Iñurritegui[a], Ignacio Gonzalez-Perez[b,*], Aitor Arana[a], Jon Larrañaga[a], Ibai Ulacia[a]

[a] Mondragon Unibertsitatea, Department of Mechanical and Industrial Production, Arrasate-Mondragon, Pais Vasco, SPAIN
[b] Universidad Politécnica de Cartagena, Department of Mechanical Engineering, Materials and Manufacturing, Cartagena, Murcia, SPAIN

ARTICLE INFO

Article history:
Received 24 March 2021
Revised 18 May 2021
Accepted 21 May 2021
Available online 10 June 2021

Keywords:
Spherical gear coupling
Gear geometry
Undercutting
Tooth contact analysis
High misalignment

ABSTRACT

Spherical gear couplings are a type of toothed coupling where the external spline usually requires highly crowned tooth surfaces to absorb high misalignments. The teeth of the external spline (or hub) may present cross sections with undercutting, particularly when the tooth number is small and the hub teeth are manufactured directly on a shaft. These peculiarities make it difficult to generate accurate hub geometries with the existing models in the literature. This paper proposes a method of generation of the hub tooth surfaces by a hob thread surface, simulating the hobbing process of the external spline and generating undercut profiles. The proposed hub model is compared with existing models where a cutting edge is considered as a generating tool of the hub. The comparison shows that the normal deviations between the hub tooth surfaces of the considered models are significant, especially when high misalignments (typically above 3°) are present and highly crowned tooth surfaces are required. Differences in the location where undercut profiles appear are also observed between the proposed model and those of the literature. Moreover, from the application of unloaded tooth contact analysis and clearance determination, disparities are observed when a misalignment angle is present.

1. Introduction

Gear couplings are widely used to transmit power between shafts due to their high power density compared to other non-splined connections [1]. Spherical gear couplings are specifically designed to work with high misalignments. Thus, they require tooth surfaces with considerable longitudinal crowning to obtain a favorable contact pattern when severe conditions of misalignment are present, typically above 3° and up to 10°. In addition, longitudinal crowning is needed to avoid interference and balance the clearance between the hub and the sleeve teeth, while increasing the contact ratio [2]. Indeed, misalignment failures account for approximately 20% of common crowned gear coupling failures [3]. Fig. 1 shows a typical spherical gear coupling featuring a hub with highly crowned tooth surfaces.

Most of the studies related to gear couplings in the scientific literature are limited to working conditions with misalignments below 3°. Among others, Alfares et al. [2] concluded that coupling misalignment due to manufacture and assembly errors is the main factor to determine tooth clearance distribution. Baker [4] experimentally analyzed the durability of cou-

* Corresponding author.
E-mail address: ignacio.gonzalez@upct.es (I. Gonzalez-Perez).

https://doi.org/10.1016/j.mechmachtheory.2021.104408
0094-114X/

Nomenclature

a_p	parabola coefficient
F_w	hob face width
h_a	rack addendum
h_f	rack dedendum
h_{ha}	hub addendum
h_{hf}	hub dedendum
h_t	hub tip height
h_{wa}	hob addendum
m	module
N_h	hub/sleeve tooth number
N_s	shaper tooth number
N_w	hob thread number
p	screw parameter
p_{ax}	hob axial pitch
r_g	sleeve pitch radius
r_h	hub pitch radius
r_s	shaper pitch radius
r_w	hob pitch radius
r_α	hub tip radius
r_β	tool path radius
s_w	hob displacement during hub generation
u	profile surface parameter
v	lead surface parameter
α	pressure angle
γ	misalignment angle
Δ_{hw}	Vertical displacement of the hob duringgeneration
δ	hob lead parameter
η	hob tip parameter
λ_w	hob lead angle
μ	angle along hob tool path
ρ	hub profile radius
ρ_{edge}	hob tip radius
ϕ_s	shaper rotation during sleeve generation
ϕ_w	hob rotation during hub generation
χ_g	sleeve generating shift coefficient
χ_h	hub generating shift coefficient
ψ_g	generation parameter of the sleeve
ψ_h	generation parameter of the hub
ψ_s	generation parameter of the shaper
ψ_w	generation parameter of the hob

plings with different lubricants and coatings up to a 0.5° misalignment angle, showing a variation of wear mechanism leading to fatigue cracks when misalignment increases. Later, Cuffaro et al. [5] designed a test rig to analyze fretting wear phenomena in aerospace applications up to a 0.2° misalignment angle. Hong et al. [6] developed a finite element model to quantify load distribution variation caused by misalignments until 0.12°, and observed a load concentration at the end of the coupling due to the effect of the tilting moment. They also demonstrated that this effect could be reduced with a proper lead crown modification value. Guo et al. [7] proposed an analytical model to determine the local contact characteristics, which proved that misalignment causes a decrease in the number of teeth in contact, leading to load increase in those in contact. All of these works are focused on the influence of several parameters in contact conditions and load distribution for small misalignments. However, uncertainty still exists in gear coupling behavior for high misalignment applications.

It is true that high misalignments, above 3°, may limit power capacity, but some machinery requires spherical gear couplings to work with high misalignments. Mancuso [8] described the use of gear spindles in heavy duty, high torque applications for a maximum misalignment angle of 6°, while Herbstritt et al. [9] discussed the design optimization of mill spindles up to 3° misalignment. In fact, the metal rolling mills industry is the main sector of application of spherical gear couplings [10], where the small size of the rolls involves working conditions up to 7°, as investigated by Larrañaga et al. [11].

Spherical gear couplings require accurate geometry generation methods to ensure a solid foundation for further investigations, such as tooth contact and clearance, or stress analyses. Employed methods of manufacturing the hub include either

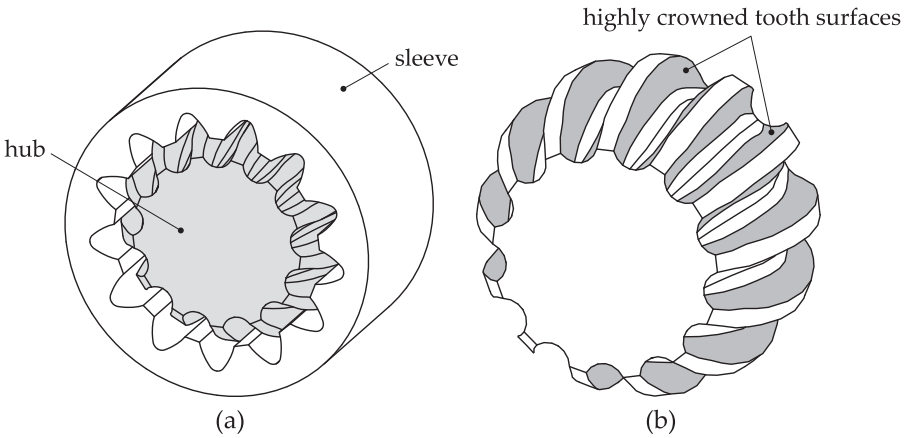

Fig. 1. Spherical gear coupling: (a) assembly of hub and sleeve, and (b) hub with highly crowned tooth surfaces.

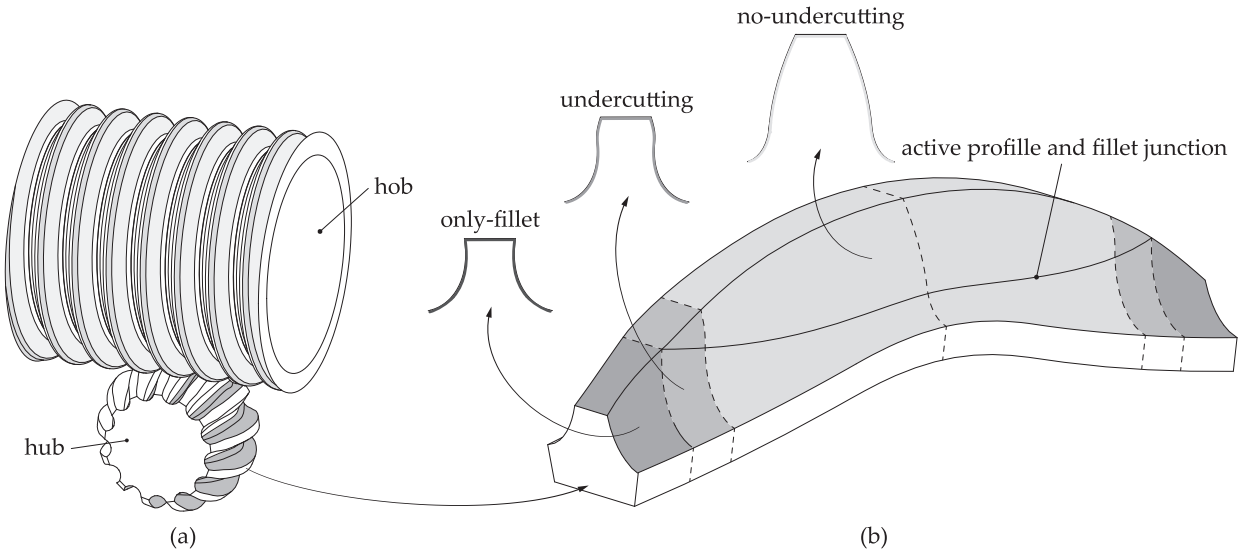

Fig. 2. Generation by a hob: (a) manufacturing of the hub by means of the hob, and (b) types of cross sections in a highly crowned hub tooth.

generation by a disk or by a hob [3,12]. Although generation by a hob (Fig. 2(a)) represents the main procedure of hub cutting, most of the generation methods presented in the literature for gear couplings simplify the hobbing process using a cutting edge. Mitome et al. [13] and Guan et al. [3] simplified the hobbing process by the rotation of the hob middle cross section. However, this method does not allow the existence of undercut profiles when reduced tool path radii are used. On the other hand, Chao et al. [14] and Kelemen et al. [15] considered the path of the cutting edge of the hob middle cross section to obtain the generating tooth surface. None of these methods has a straightforward methodology to be easily adapted to different tool paths of the hob.

Although the methods mentioned above can be accurate for small amounts of crowning, higher crowning values demand exact generation methods, and therefore the geometry of the generating tool surface must be assessed. A hob may be regarded as a set of cutting edges distributed along its thread, and as a result the thread surface has to be considered in the model of the cutting tool to achieve an accurate generation method.

Generation of a gear tooth surface by a hob (or a worm) thread surface was introduced by Litvin et al. [16,17] and employed in some works, such as, generation of face-gear drives [18,19], noncircular gears [20,21] or screw rotors [22]. Later, Jia et al. [23] applied a discrete enveloping method considering a hob among different gear tools. Furthermore, Vedmar [24] investigated the roughness of hobbed gear tooth surfaces and Klocke et al. [25] introduced gear tooth surface deviations caused by a non-ideal hobbing simulation.

However, the amount of crowning that may be required in gear drives is much lower than in spherical gear couplings (see Fig. 1(b)). Thus, their generation introduces new problems including the appearance of singularities. As stated in [17], the appearance of singular points on the generated surface is the warning that the surface may be undercut during the

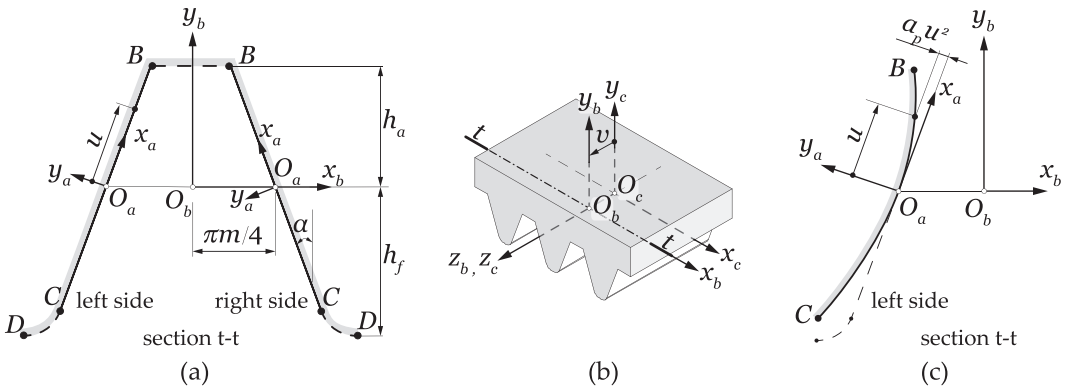

Fig. 3. Rack-cutter tooth surface Σ_c definition: (a) surface parameter u, (b) surface parameter v, and (c) definition of profile crowning.

generation process. Indeed, the existence of undercutting is unavoidable, especially in small parts where the hub teeth are manufactured directly on a shaft [26]. As a consequence, different regions along the length of the tooth can be observed in Fig. 2(b).

Therefore, the main goals of the present research are:

(1) To numerically generate spherical hub tooth surfaces by a hob thread surface, and implement an algorithm for the detection of singularities during the generation process. The proposed generation method identifies three types of cross sections in the generated teeth of the hub (Fig. 2(b)): (i) cross sections where no undercutting exists, (ii) cross sections where the active profile is undercut and coexists with the fillet, and (iii) cross sections where only the fillet exists. Detection of undercutting is important for a better estimation of the bending strength of the hub in further stress analyses.

(2) To compare the hub generation model with two simplified models where the hob thread surface is substituted by a set of cutting edges. These two simplified methods of hub generation by a hob are described in detail in [3,15] and are implemented in this work for the purpose of comparison. The developed algorithm for the detection of singularities is also implemented in these simplified methods. The comparison is based on the determination of normal deviations between the hub tooth surface of the proposed model and the hub tooth surface of the simplified ones. In addition, differences in the location of undercut profiles are investigated.

(3) To analyze unloaded tooth contact when a misalignment angle is present and to determine the clearance between the pairs of teeth of the spherical gear coupling. To this end, a sleeve model is obtained through the computational generation of the sleeve tooth surfaces by a shaper tooth surface.

2. Generation of the hub model

Generation of the hub tooth surface Σ_h by a hob requires prior determination of the hob (or worm) thread surface Σ_w (Secs. 2.2, 2.3). For that purpose, a standard rack-cutter tooth surface Σ_c is defined (Section 2.1) as the generating surface of Σ_w. Once the process to determine the surface Σ_h is described (Section 2.4), an algorithm for the determination of singularities and the location of different types of cross sections in the hub teeth is presented (Section 2.5). Finally, two existing procedures to determine the surface Σ_h are provided (Section 2.6) for the purpose of comparison.

2.1. Definition of the rack-cutter tooth surface Σ_c

Three coordinate systems are considered for the definition of the surface Σ_c as is illustrated in Fig. 3: (i) the system S_a is attached to the rack-cutter profile and allows the surface parameter u to be defined, (ii) the system S_b is located with its origin O_b at a distance $\pi m/4$ from the origin O_a, where m is the module of the gear coupling, and (iii) the system S_c allows the other surface parameter, v, to be defined by locating the origin O_b and coordinate axes x_b and y_b at section $t-t$ (Fig. 3(b)).

The rack-cutter tooth surface Σ_c is obtained in the system S_c as

$$\mathbf{r}_c(u,v) = \mathbf{M}_{cb}(v)\mathbf{M}_{ba}\mathbf{r}_a(u) \tag{1}$$

$$\mathbf{r}_c(u,v) = \begin{bmatrix} 1 & 0 & 0 & 0 \\ 0 & 1 & 0 & 0 \\ 0 & 0 & 1 & v \\ 0 & 0 & 0 & 1 \end{bmatrix} \cdot \begin{bmatrix} \mp\sin\alpha & \mp\cos\alpha & 0 & \pm\dfrac{\pi m}{4} \\ \cos\alpha & \mp\sin\alpha & 0 & 0 \\ 0 & 0 & 1 & 0 \\ 0 & 0 & 0 & 1 \end{bmatrix} \cdot \begin{bmatrix} u \\ 0 \\ 0 \\ 1 \end{bmatrix} \tag{2}$$

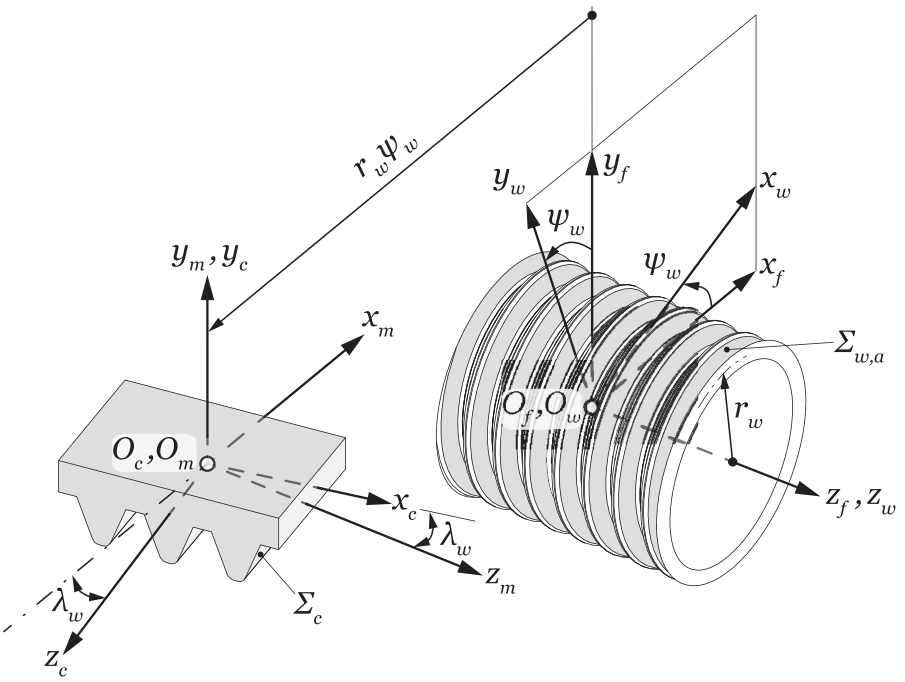

Fig. 4. Determination of the active hob thread surface $\Sigma_{w,a}$.

where α is the pressure angle of the coupling. The upper sign is applied to the right side whereas the lower sign is applied to the left side of the rack-cutter tooth.

When profile crowning is required to avoid edge contact at the tips of the hub and sleeve teeth (Fig. 3(c)), the vector $\mathbf{r}_a(u)$ is obtained as

$$\mathbf{r}_a(u) = [u \quad a_p u^2 \quad 0 \quad 1]^T \tag{3}$$

where a_p is a parabola coefficient.

2.2. Generation of the active hob thread surface $\Sigma_{w,a}$

Fig. 4 shows the coordinate systems that are considered to determine the active hob thread surface $\Sigma_{w,a}$. The coordinate systems S_w and S_c are rigidly connected to the hob and the rack-cutter, respectively. The system S_f is a fixed coordinate system where the rotation of the hob is taken into consideration through the angle ψ_w. The system S_m is an auxiliary coordinate system attached to the rack-cutter that allows the cutter to be positioned on the hob using the lead angle λ_w. The systems S_m and S_c are displaced the value $\psi_w r_w$ in the direction of the axis x_m, which is parallel to the axis x_f. Here, r_w is the pitch radius of the hob and coincides with the shortest distance between the axis x_m and x_f.

The surface $\Sigma_{w,a}$ can be determined as the envelope to the family of generating tooth surfaces Σ_c in the system S_w by simultaneous consideration of the following equations

$$\mathbf{r}_w(u, v, \psi_w) = \mathbf{M}_{wc}(\psi_w)\mathbf{r}_c(u, v) \tag{4}$$

$$f_1(u, v, \psi_w) = \left(\frac{\partial \mathbf{r}_w}{\partial u} \times \frac{\partial \mathbf{r}_w}{\partial v}\right) \cdot \frac{\partial \mathbf{r}_w}{\partial \psi_w} = 0 \tag{5}$$

where

$$\begin{aligned}\mathbf{M}_{wc} &= \mathbf{M}_{wf}\mathbf{M}_{fm}\mathbf{M}_{mc} \\ &= \begin{bmatrix} \cos\psi_w & \sin\psi_w & 0 & 0 \\ -\sin\psi_w & \cos\psi_w & 0 & 0 \\ 0 & 0 & 1 & 0 \\ 0 & 0 & 0 & 1 \end{bmatrix} \cdot \begin{bmatrix} 1 & 0 & 0 & -r_w\psi_w \\ 0 & 1 & 0 & r_w \\ 0 & 0 & 1 & 0 \\ 0 & 0 & 0 & 1 \end{bmatrix} \cdot \begin{bmatrix} \sin\lambda_w & 0 & -\cos\lambda_w & 0 \\ 0 & 1 & 0 & 0 \\ \cos\lambda_w & 0 & \sin\lambda_w & 0 \\ 0 & 0 & 0 & 1 \end{bmatrix}\end{aligned} \tag{6}$$

and $f_1(u, v, \psi_w) = 0$ is the equation of meshing.

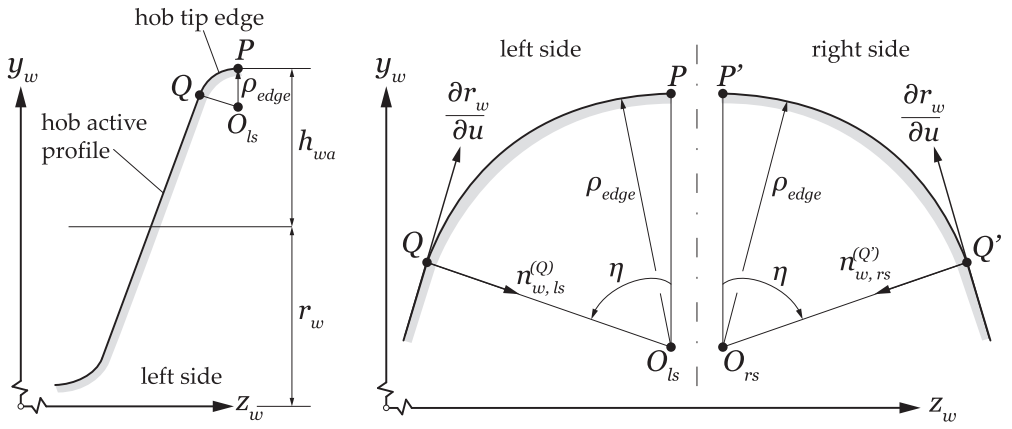

Fig. 5. Definition of the hob tip edge.

2.3. Determination of the tip edge surface $\Sigma_{w,t}$ of the hob thread

The surface $\Sigma_{w,t}$ is built directly on the system S_w as a helicoid with surface parameters η and δ. The tip edge is first defined on the plane $x_w = 0$ (Fig. 5). Points Q and Q' are the left and right joint points between the active profile and the tip edge of the hob thread at each side. The unit normals $\mathbf{n}^{(Q)}_{w,ls}$ and $\mathbf{n}^{(Q')}_{w,rs}$ can be obtained on the plane (y_w, z_w) as

$$\mathbf{n}^{(Q)}_{w,ls} = \mathbf{i}_w \times \frac{\frac{\partial \mathbf{r}_w}{\partial u}|_{u=u_Q}}{\left|\frac{\partial \mathbf{r}_w}{\partial u}|_{u=u_Q}\right|} \tag{7}$$

$$\mathbf{n}^{(Q')}_{w,rs} = -\mathbf{i}_w \times \frac{\frac{\partial \mathbf{r}_w}{\partial u}|_{u=u_{Q'}}}{\left|\frac{\partial \mathbf{r}_w}{\partial u}|_{u=u_{Q'}}\right|} \tag{8}$$

The following condition determines the parameter u_Q (and $u_{Q'}$) of the point Q (and Q')

$$y_w + n_{w,y}\rho_{edge} = r_w + h_{wa} - \rho_{edge} \tag{9}$$

where h_{wa} is the addendum and ρ_{edge} is the tip edge radius of the hob.

The center points O_{ls} and O_{rs} are then computed as

$$\mathbf{r}^{(O_{ls})}_w = \mathbf{r}^{(Q)}_w + \rho_{edge}\mathbf{n}^{(Q)}_{w,ls} \tag{10}$$

$$\mathbf{r}^{(O_{rs})}_w = \mathbf{r}^{(Q')}_w + \rho_{edge}\mathbf{n}^{(Q')}_{w,rs} \tag{11}$$

Next, the tip edges are defined as

$$\mathbf{r}^{(ls)}_w = \mathbf{r}^{(O_{ls})}_w + \rho_{edge}[0 \quad \cos\eta \quad -\sin\eta \quad 1]^T \tag{12}$$

$$\mathbf{r}^{(rs)}_w = \mathbf{r}^{(O_{rs})}_w + \rho_{edge}[0 \quad \cos\eta \quad +\sin\eta \quad 1]^T \tag{13}$$

where

$$\eta_{min} \le \eta \le \eta_{max} \quad \eta_{min} = 0 \quad \eta_{max} = \arccos(-\mathbf{n}^{(Q)}_{w,ls} \cdot \mathbf{j}_w) \tag{14}$$

To define the tip edge surface of the hob thread as a helicoid, a screw motion is applied to the previously determined tip edge considering the screw parameter p,

$$p = \frac{p_{ax}N_w}{2\pi} \tag{15}$$

where p_{ax} is the axial pitch of the hob and N_w the number of threads of the hob.

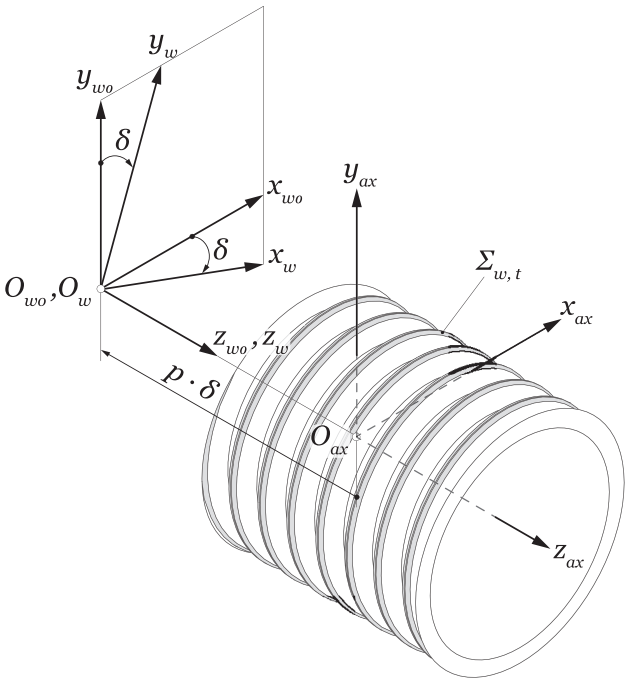

Fig. 6. Derivation of the tip edge surface $\Sigma_{w,t}$ of the hob thread.

Fig. 6 shows an auxiliary fixed coordinate system S_{ax} that coincides with the system S_w when $\delta = 0$. Prior to the screw motion, the tip edges derived in Eqs. (12), (13) are computed in the system S_{ax} as

$$\mathbf{r}_{\mathrm{ax}}(\eta) = [0 \quad y_w(\eta) \quad z_w(\eta) \quad 1]^T \tag{16}$$

Each thread side is considered independently, but indexes *ls* and *rs* are omitted for the purpose of simplicity.

The screw motion implies a rotation δ and a displacement $p\delta$ of the coordinate system S_w with respect to the coordinate system S_{ax} (Fig. 6). The system S_{wo} is another auxiliary coordinate system that displaces with the system S_w but does not rotate. Finally, the tip edge surface $\Sigma_{w,t}$ of the hub thread is determined as

$$\mathbf{r}_{\mathrm{w}}(\delta, \eta) = \mathbf{M}_{\mathrm{w,ax}}(\delta)\mathbf{r}_{\mathrm{ax}}(\eta) = \begin{bmatrix} \cos\delta & \mp\sin\delta & 0 & 0 \\ \pm\sin\delta & \cos\delta & 0 & 0 \\ 0 & 0 & 1 & p\delta \\ 0 & 0 & 0 & 1 \end{bmatrix} \mathbf{r}_{\mathrm{ax}}(\eta) \tag{17}$$

Here, the upper sign is applied to a hob with a right hand helix whereas the lower sign is for a hob with a left hand helix.

2.4. Generation of the hub tooth surface Σ_h

The hub tooth surface Σ_h is composed of the active tooth surface $\Sigma_{h,a}$, and the fillet tooth surface $\Sigma_{h,f}$. The surface $\Sigma_{h,a}$ is generated by the active hob thread surface $\Sigma_{w,a}$, and the surface $\Sigma_{h,f}$ is generated by the tip edge surface $\Sigma_{w,t}$ of the hob thread. Fig. 7 shows the coordinate systems that are involved in the generation process. The system S_f is a fixed coordinate system where rotation of the hub occurs. The auxiliary coordinate systems S_p and S_n displace with the hob through a curved tool path of radius r_β. The system S_p allows the system S_n to be positioned considering the lead angle of the hob λ_w, which is given as

$$\lambda_w = \arctan \frac{p_{ax} N_w}{2\pi r_w} \tag{18}$$

The system S_w, rigidly connected to the hob, moves with the systems S_p and S_n, and in addition rotates the angle ϕ_w. Similarly, the system S_h is rigidly connected to the hub and rotates the angle ψ_h, which is given as

$$\psi_h = \phi_w \frac{N_w}{N_h} \tag{19}$$

where N_h is the number of teeth of the hub.

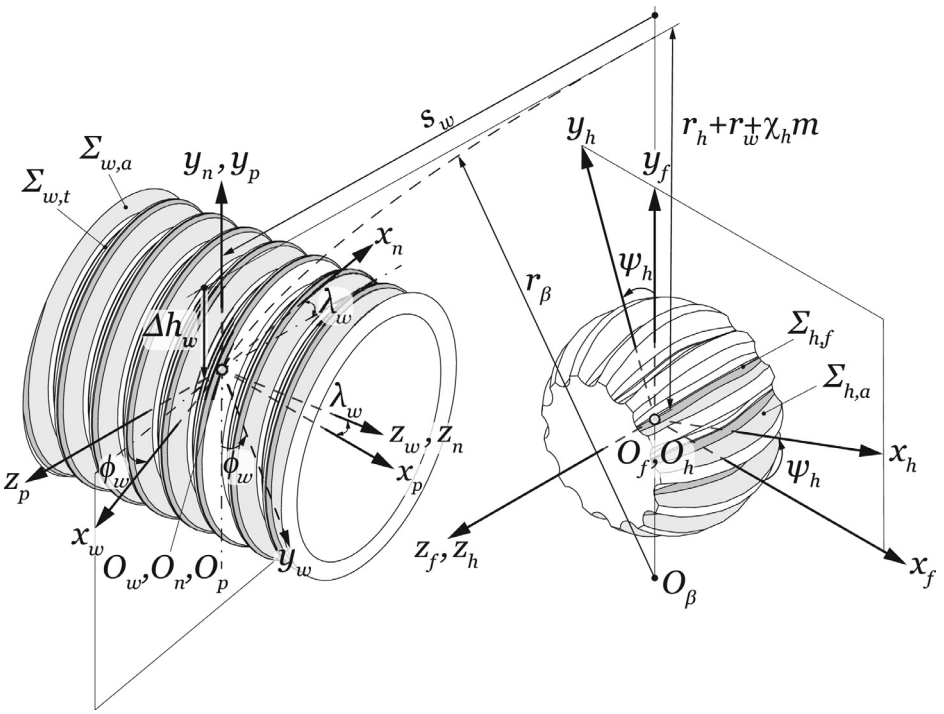

Fig. 7. Derivation of the hub tooth surfaces $\Sigma_{h,a}$ and $\Sigma_{h,f}$.

The generation is considered as a double-enveloping process [17], represented with two independent parameters, ϕ_w and s_w. To determine the active hub tooth surface $\Sigma_{h,a}$, coordinate transformation from system S_w to system S_h

$$\mathbf{r}_{\mathrm{h,a}}(u, v, \psi_w, s_w, \phi_w) = \mathbf{M}_{\mathrm{hw}}(s_w, \phi_w)\mathbf{r}_{\mathrm{w}}(u, v, \psi_w) \tag{20}$$

and corresponding equations of meshing (Eqn 21, 22 and 23–23) are solved.

$$f_1(u, v, \psi_w) = \left(\frac{\partial \mathbf{r}_{\mathrm{w}}}{\partial u} \times \frac{\partial \mathbf{r}_{\mathrm{w}}}{\partial v}\right) \cdot \frac{\partial \mathbf{r}_{\mathrm{w}}}{\partial \psi_w} = 0 \tag{21}$$

$$f_2(u, v, s_w, \phi_w) = \left(\frac{\partial \mathbf{r}_{\mathrm{h,a}}}{\partial u} \times \frac{\partial \mathbf{r}_{\mathrm{h,a}}}{\partial v}\right) \cdot \frac{\partial \mathbf{r}_{\mathrm{h,a}}}{\partial \phi_w} = 0 \tag{22}$$

$$f_3(u, v, s_w, \phi_w) = \left(\frac{\partial \mathbf{r}_{\mathrm{h,a}}}{\partial u} \times \frac{\partial \mathbf{r}_{\mathrm{h,a}}}{\partial v}\right) \cdot \frac{\partial \mathbf{r}_{\mathrm{h,a}}}{\partial s_w} = 0 \tag{23}$$

Likewise, the fillet hub tooth surface $\Sigma_{h,f}$ can be determined with the same coordinate transformation

$$\mathbf{r}_{\mathrm{h,f}}(\eta, \delta, s_w, \phi_w) = \mathbf{M}_{\mathrm{hw}}(s_w, \phi_w)\mathbf{r}_{\mathrm{w}}(\eta, \delta) \tag{24}$$

and corresponding equations of meshing (25,26).

$$f_4(\eta, \delta, s_w, \phi_w) = \left(\frac{\partial \mathbf{r}_{\mathrm{h,f}}}{\partial \eta} \times \frac{\partial \mathbf{r}_{\mathrm{h,f}}}{\partial \delta}\right) \cdot \frac{\partial \mathbf{r}_{\mathrm{h,f}}}{\partial \phi_w} = 0 \tag{25}$$

$$f_5(\eta, \delta, s_w, \phi_w) = \left(\frac{\partial \mathbf{r}_{\mathrm{h,f}}}{\partial \eta} \times \frac{\partial \mathbf{r}_{\mathrm{h,f}}}{\partial \delta}\right) \cdot \frac{\partial \mathbf{r}_{\mathrm{h,f}}}{\partial s_w} = 0 \tag{26}$$

The matrix $\mathbf{M}_{\mathrm{hw}}(s_w, \phi_w)$ is given by $\mathbf{M}_{\mathrm{gw}} = \mathbf{M}_{\mathrm{hf}}\mathbf{M}_{\mathrm{fp}}\mathbf{M}_{\mathrm{pn}}\mathbf{M}_{\mathrm{nw}}$, where

$$\mathbf{M}_{\mathrm{hf}} = \begin{bmatrix} \cos\psi_h & \sin\psi_h & 0 & 0 \\ -\sin\psi_h & \cos\psi_h & 0 & 0 \\ 0 & 0 & 1 & 0 \\ 0 & 0 & 0 & 1 \end{bmatrix} \quad \mathbf{M}_{\mathrm{fp}} = \begin{bmatrix} 1 & 0 & 0 & 0 \\ 0 & 1 & 0 & r_h + r_w + \chi_h m - \Delta h_w \\ 0 & 0 & 1 & s_w \\ 0 & 0 & 0 & 1 \end{bmatrix} \tag{27}$$

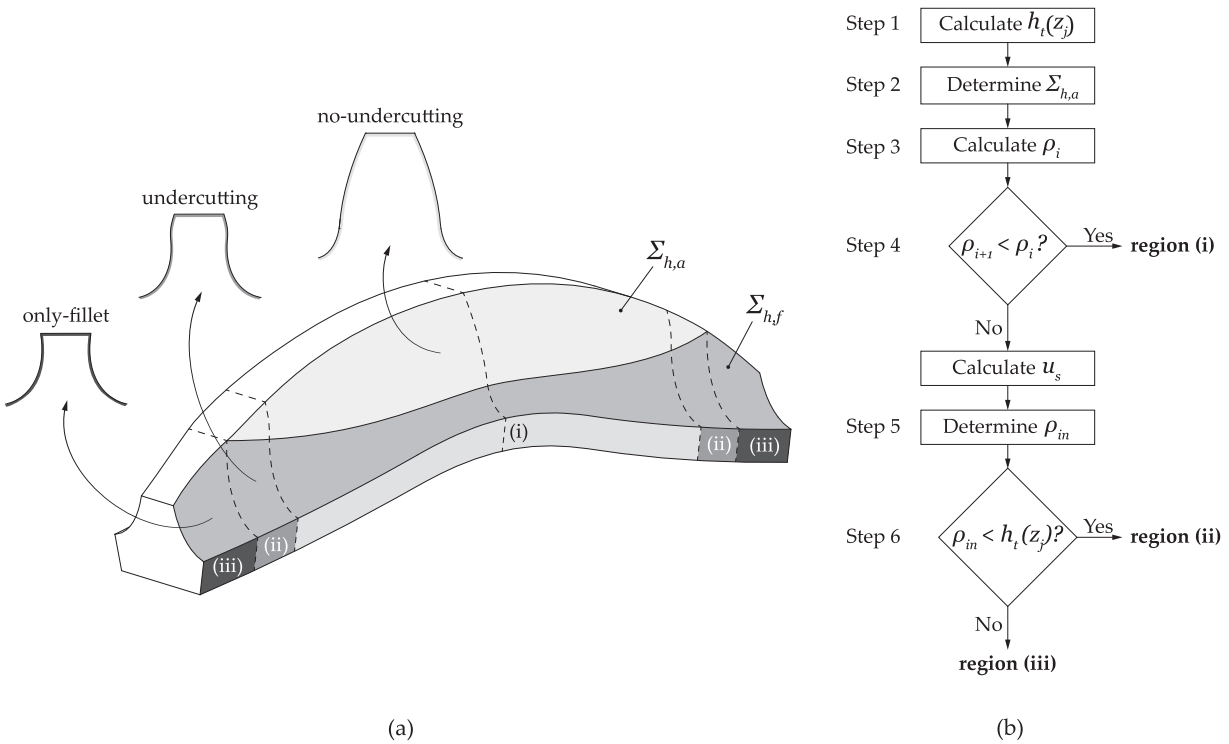

Fig. 8. Hub tooth geometry: (a) different types of cross sections, and (b) algorithm to detect undercutting and identify the region for each cross section.

$$\mathbf{M}_{\text{pn}} = \begin{bmatrix} -\sin\lambda_w & 0 & \cos\lambda_w & 0 \\ 0 & 1 & 0 & 0 \\ -\cos\lambda_w & 0 & -\sin\lambda_w & 0 \\ 0 & 0 & 0 & 1 \end{bmatrix} \quad \mathbf{M}_{\text{nw}} = \begin{bmatrix} -\cos\phi_w & \sin\phi_w & 0 & 0 \\ -\sin\phi_w & -\cos\phi_w & 0 & 0 \\ 0 & 0 & 1 & 0 \\ 0 & 0 & 0 & 1 \end{bmatrix} \tag{28}$$

Here, r_h is the pitch radius of the hub, χ_h is a generating shift coefficient, and $\Delta h_w = r_\beta - \sqrt{r_\beta^2 - s_w^2}$ represents the plunging of the hob when a circular tool path is applied. A negative generating shift coefficient is usually considered when some backlash between the hub and the sleeve teeth is required.

2.5. Singularities in the generation of the hub tooth surface Σ_h

When the hub comprises highly crowned tooth surfaces, an algorithm to detect undercutting is required to generate the hub teeth with different types of cross sections as illustrated in Fig. 8(a). This algorithm allows to detect three different types of cross sections and determine the interval of values for the profile and fillet parameters at each type of cross section. The three different types of cross sections in the hub tooth surface Σ_h are shown in Fig. 8(a): (i) a no-undercutting region where tangency between the surfaces $\Sigma_{h,a}$ and $\Sigma_{h,f}$ is observed, (ii) an undercutting region where the tangency between $\Sigma_{h,a}$ and $\Sigma_{h,f}$ is not observed, and (iii) an only-fillet region where just the surface $\Sigma_{h,f}$ exists. The only-fillet and undercutting regions can be prevented by shortening the face width of the hub or by increasing the tool path radius r_β. Nevertheless, such options are not possible in some hub designs, where space is a constraint and the teeth are manufactured directly on a shaft with highly crowned tooth surfaces to absorb high misalignments [26].

The following algorithm (Fig. 8(b)) was applied to each cross section of the hub tooth to identify its region and determine its geometry:

Step 1 The coordinate z_j, $j = \{1, \ldots, n_j\}$, of the hub tooth is given for each cross section j of a total of n_j sections. The hub tip height $h_t(z_j)$ is determined at each cross section (Fig. 9)

$$h_t(z_j) = r_h + h_{ha} - r_\alpha[1 - \cos\mu(z_j)] \tag{29}$$

where $r_\alpha = r_\beta - r_w - \chi_h m + h_{ha}$ and $\mu(z_j) = \arcsin\left(\frac{z_j}{r_\alpha}\right)$. Here, h_{ha} is the hub addendum.

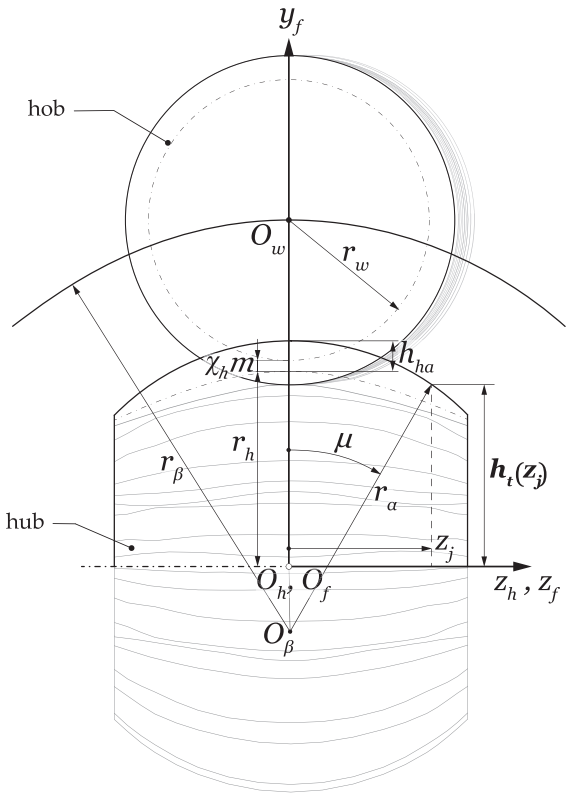

Fig. 9. Derivation of the hub tip height h_t.

Step 2 Variation of the surface parameter u determines the active profile of the cross section considering the following set of equations

$$\begin{aligned}\mathbf{r}_{\mathrm{h,a}}(u,v,\psi_w,s_w,\phi_w) &= \mathbf{M}_{\mathrm{hw}}(s_w,\phi_w)\mathbf{r}_{\mathrm{w}}(u,v,\psi_w)\\ f_1(u,v,\psi_w) &= 0\\ f_2(u,v,s_w,\phi_w) &= 0\\ f_3(u,v,s_w,\phi_w) &= 0\\ f_6(u,v,\psi_w,s_w,\phi_w) &= z_h - z_j = 0\end{aligned} \tag{30}$$

Equations $f_1 = 0$, $f_2 = 0$ and $f_3 = 0$ correspond to equations (21), (22) and (23), respectively.

Step 3 The tooth profile radii ρ_i, $i = \{1,\ldots,n_i\}$, are computed considering n_i points along the active profile of the cross section. The surface parameter u is varied from $u_{\min}$ (at the tip of the hub tooth) to $u_{\max}$ (at the bottom of the hub profile). Thus, Fig. 10(a) shows how the radii are computed from the tip to the bottom of the active profile as $\rho_i = \sqrt{x_h^2 + y_h^2}$ with $\rho_{i+1} < \rho_i$.

Step 4 When $\rho_{i+1} < \rho_i$, the active profile is free of singularities and the cross section of the tooth is located in the no-undercutting region (i). In the case that $\rho_{i+1} \geq \rho_i$, tangency no longer exists between the active profile and the fillet due to the presence of a second branch (Fig. 10(b)). For the first occurrence i in which $\rho_{i+1} \geq \rho_i$, the parameter u_s of the singular point is obtained.

Step 5 In the case of singularity existence, intersection between the active profile and the fillet (Fig. 10(b)) is determined as follows:

(a) Set of equations (30) represent the active profile of the cross section with surface parameter $u_{\min} \leq u \leq u_s$.

(b) A second set of equations (31) represent the fillet profile of the cross section with surface parameter $\eta_{\min} \leq \eta \leq \eta_{\max}$

$$\begin{aligned}\mathbf{r}_{\mathrm{h,f}}(\eta,\delta,s_w,\phi_w) &= \mathbf{M}_{\mathrm{hw}}(s_w,\phi_w)\mathbf{r}_{\mathrm{w}}(\eta,\delta)\\ f_4(\eta,\delta,s_w,\phi_w) &= 0\\ f_5(\eta,\delta,s_w,\phi_w) &= 0\\ f_7(\eta,\delta,s_w,\phi_w) &= z_h - z_j = 0\end{aligned} \tag{31}$$

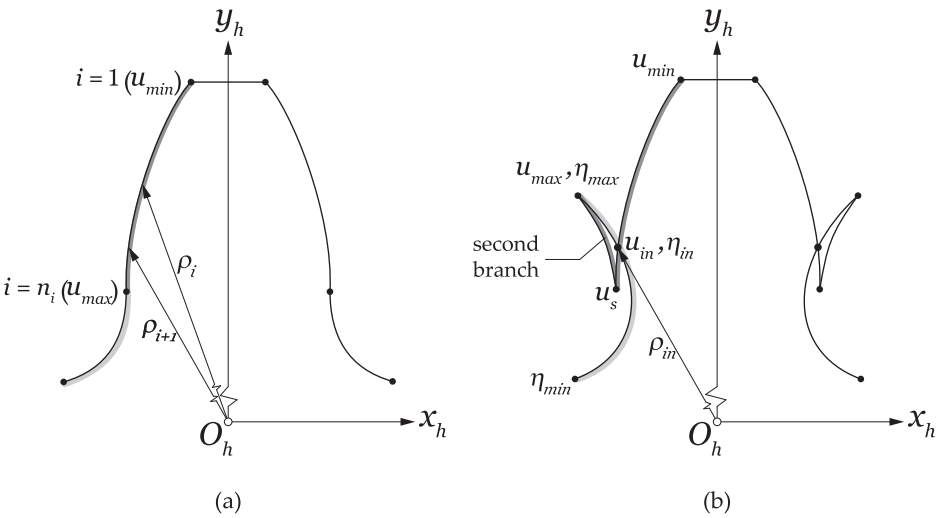

Fig. 10. Hub tooth cross section: (a) without undercutting, and (b) with undercutting.

Equations $f_4 = 0$ and $f_5 = 0$ correspond to equations (25) and (26), respectively.

(c) The intersection of the active and fillet profiles solving both sets of equations, (30) and (31), enables surface parameters u_{in} and η_{in} to be determined.

(d) The corresponding radius of the intersection point between the active profile and the fillet is established as $\rho_{in} = \sqrt{[x_h(u_{in})]^2 + [y_h(u_{in})]^2}$.

Step 6 When $\rho_{in} < h_t(z_j)$, the cross section will be located in the undercutting region (ii), where the active profile is generated with $u_{\min} \le u \le u_{in}$, and the fillet profile with $\eta_{\min} \le \eta \le \eta_{in}$. In contrast, if $\rho_{in} \ge h_t(z_j)$ the cross section will be located in the only-fillet region (iii). In this case, the fillet is generated with $\eta_{\min} \le \eta \le \eta'_{\max}$, where $\eta'_{\max}$ is determined by simultaneous consideration of the set of equations (31) and the following additional equation

$$f_8(\eta, \delta, s_w, \phi_w) = x_h^2 + y_h^2 - h_t^2(z_j) = 0 \tag{32}$$

2.6. Simplified models for generation of the hub

Two simplified models presented in the literature for the generation of a hub by a hob have been implemented for the purpose of comparison with the proposed model.

2.6.1. Model 1

The first model is described in [15] and illustrated in Fig. 11. A cutting edge is defined considering the profile parameter u in the coordinate system S_c. The system S_c is rigidly connected to the auxiliary system S_m, and rotates the angle θ around axis x_m. Parameters u and θ define a generating surface Σ_o in the coordinate system S_o. The displacement $r_h\psi_h$ of the surface Σ_o, rigidly connected to the system S_o, is accompanied by the rotation ψ_h of the hub. This model obtains the hub tooth surface in a single-enveloping process, with ψ_h as the generalized parameter of generation in accordance with the theory of gearing [17].

2.6.2. Model 2

The second model is reported in [3] and [15] and illustrated in Fig. 12. In this case, the hub tooth surface is obtained as a set of independent cross sections, each one generated by a cutting edge defined in the coordinate system S_{ci}. For the positioning of each cutting edge over the hub, a different generating shift coefficient χ_i is used. The displacement $r_h\psi_{hi}$ of the cutting edge is accompanied by the rotation ψ_{hi} of the hub. Each hub tooth profile i is obtained in a single-enveloping process with ψ_{hi} as the generalized parameter of generation. This is also a single enveloping process [17]. In this model, derivation of the normal of the hub tooth surface is not straightforward and requires consideration of u and z_i as surface parameters of the theoretical generating tool surface.

3. Unloaded tooth contact and clearance analyses

Unloaded tooth contact and clearance analyses of the gear coupling are carried out assuming that a misalignment γ is present between the sleeve and the hub. The sleeve model is based on involute tooth surfaces and can be obtained as explained in Appendix A. Fig. 13 shows a fixed coordinate system S_f where the hub and the sleeve models are assembled.

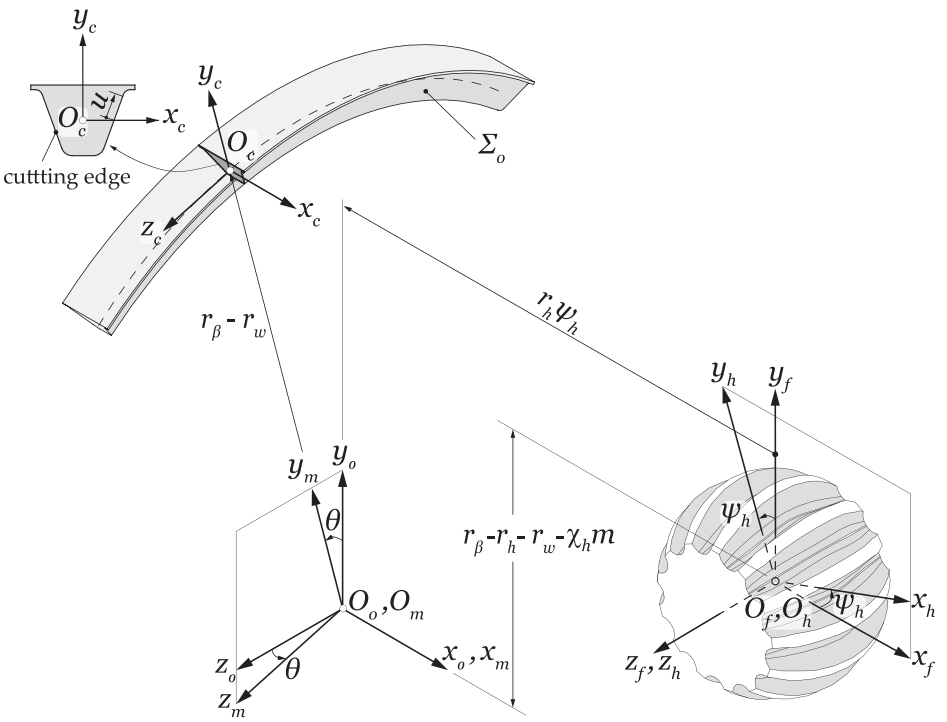

Fig. 11. Derivation of the hub tooth surface in model 1.

The systems S_h and S_g are rigidly connected to the hub and the sleeve models, respectively. The sleeve model is mounted in the system S_f with a misalignment γ around the axis y_f, which coincides with the axis y_g. While the sleeve model is held at rest, the hub model can rotate the angle ϕ_h until one of its teeth makes contact with one sleeve tooth. A counterclockwise rotation of the hub model is supposed.

Point contact is assumed between the surfaces Σ_h and Σ_g due to the double crowned tooth surfaces of the hub model. The following algorithm (divided in 8 steps) was applied to determine the contact point at one pair of teeth, and the clearance for those remaining:

Step 1 The tooth of the hub whose symmetry axis is perpendicular to the misalignment plane for $\phi_h = 0$ is assumed to be the first tooth to make contact with a tooth of the sleeve model [2]. Assuming, for the purpose of simplicity, that (u_h, v_h) are the surface parameters of surface Σ_h (located at the left side of the tooth that comes into contact), the following coordinate transformation represents the surface Σ_h in the system S_f as

$$\mathbf{r}_{\mathrm{f}}^{(\mathrm{hub})}(u_h, v_h, \phi_h) = \mathbf{M}_{\mathrm{fh}}(\phi_h)\mathbf{r}_{\mathrm{h}}(u_h, v_h) \tag{33}$$

Here,

$$\mathbf{M}_{\mathrm{fh}} = \begin{bmatrix} \cos\phi_h & \sin\phi_h & 0 & 0 \\ -\sin\phi_h & \cos\phi_h & 0 & 0 \\ 0 & 0 & 1 & 0 \\ 0 & 0 & 0 & 1 \end{bmatrix} \tag{34}$$

where ϕ_h is the angle of rotation of the hub to make contact with the sleeve. The variables (u_h, v_h, ϕ_h) are the unknowns for the sought-for contact point.

Step 2 The unit normal to surface Σ_h at the sought-for contact point can be obtained in the system S_f as

$$\mathbf{n}_{\mathrm{f}}^{(\mathrm{hub})}(u_h, v_h, \phi_h) = \mathbf{L}_{\mathrm{fh}}(\phi_h)\frac{\dfrac{\partial \mathbf{r}_{\mathrm{h}}}{\partial u_h} \times \dfrac{\partial \mathbf{r}_{\mathrm{h}}}{\partial v_h}}{\left|\dfrac{\partial \mathbf{r}_{\mathrm{h}}}{\partial u_h} \times \dfrac{\partial \mathbf{r}_{\mathrm{h}}}{\partial v_h}\right|} \tag{35}$$

where the matrix $\mathbf{L}_{\mathrm{fh}}$ is of 3×3 order and can be determined from the matrix $\mathbf{M}_{\mathrm{fh}}$ by eliminating the last row and the last column.

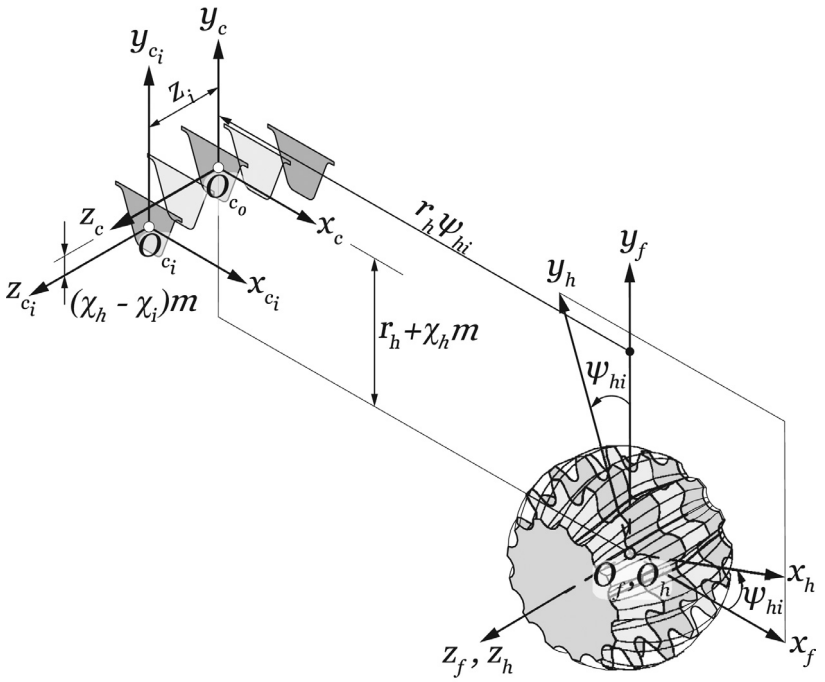

Fig. 12. Derivation of the hub cross sections in model 2.

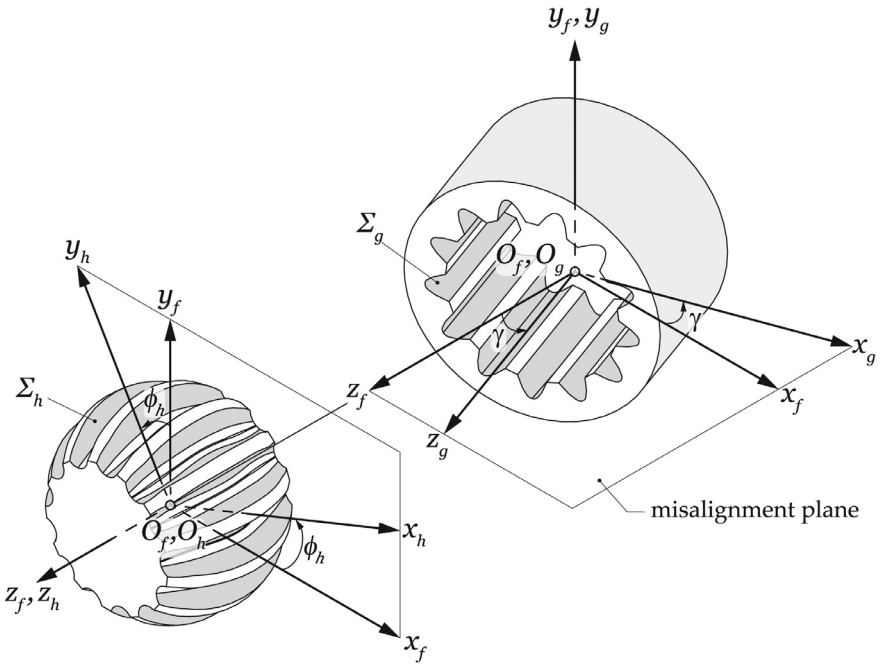

Fig. 13. Coordinate systems applied for the positioning of a gear coupling with shaft misalignment angle γ.

Step 3 The surface Σ_g, located at the left side of the tooth space whose symmetry axis is y_g, is considered to make contact with the surface Σ_h. Assuming, for the purpose of simplicity, that (u_g, v_g) are the surface parameters of the surface Σ_g, the following coordinate transformation allows the surface Σ_g to be represented in the system S_f

$$\mathbf{r}_{\mathrm{f}}^{(\mathrm{sleeve})}(u_g, v_g) = \mathbf{M}_{\mathrm{fg}}\mathbf{r}_{\mathrm{g}}(u_g, v_g) \tag{36}$$

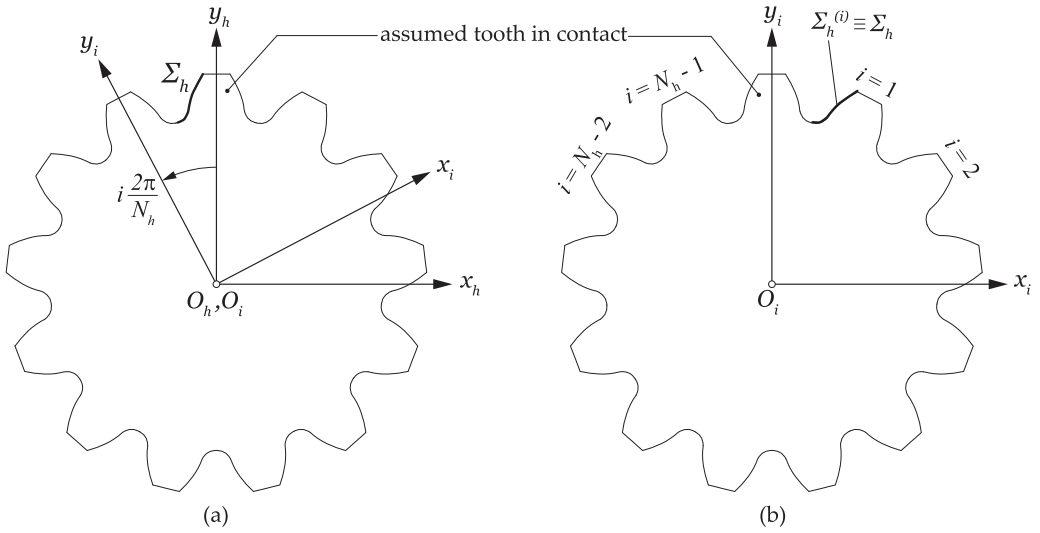

Fig. 14. Derivation of tooth surfaces $\Sigma_h^{(i)}$ at the hub.

Here,

$$\mathbf{M}_{\mathrm{fg}} = \begin{bmatrix} \cos\gamma & 0 & -\sin\gamma & 0 \\ 0 & 1 & 0 & 0 \\ \sin\gamma & 0 & \cos\gamma & 0 \\ 0 & 0 & 0 & 1 \end{bmatrix} \tag{37}$$

where (u_g, v_g) are the unknowns of the sought-for contact point.

Step 4 The unit normal to surface Σ_g at the sought-for contact point can be obtained in the system S_f as

$$\mathbf{n}_{\mathrm{f}}^{(\mathrm{sleeve})}(u_g, v_g) = \mathbf{L}_{\mathrm{fg}} \frac{\dfrac{\partial \mathbf{r}_{\mathrm{g}}}{\partial u_g} \times \dfrac{\partial \mathbf{r}_{\mathrm{g}}}{\partial v_g}}{\left| \dfrac{\partial \mathbf{r}_{\mathrm{g}}}{\partial u_g} \times \dfrac{\partial \mathbf{r}_{\mathrm{g}}}{\partial v_g} \right|} \tag{38}$$

where the matrix $\mathbf{L}_{\mathrm{fg}}$ is of 3×3 order and can be determined from the matrix $\mathbf{M}_{\mathrm{fg}}$ by eliminating the last row and the last column.

Step 5 A system of five independent scalar equations and unknowns $\{u_h, v_h, \phi_h, u_g\ v_g\}$ is defined as

$$\mathbf{r}_{\mathrm{f}}^{(\mathrm{hub})}(u_h, v_h, \phi_h) = \mathbf{r}_{\mathrm{f}}^{(\mathrm{sleeve})}(u_g, v_g) \tag{39}$$

$$\mathbf{n}_{\mathrm{f}}^{(\mathrm{hub})}(u_h, v_h, \phi_h) = \mathbf{n}_{\mathrm{f}}^{(\mathrm{sleeve})}(u_g, v_g) \tag{40}$$

Equation (40) represents only two independent scalar equations since $|\mathbf{n}_{\mathrm{f}}^{(\mathrm{hub})}| = |\mathbf{n}_{\mathrm{f}}^{(\mathrm{sleeve})}| = 1$.

Step 6 The surfaces $\Sigma_h^{(i)}$ and $\Sigma_g^{(i)}$, $i = \{1, \ldots, N_h - 1\}$, of adjacent teeth are assumed not to be in contact, since contacting tooth surfaces Σ_h and Σ_g are considered to be rigid. Clearance at each adjacent pair of teeth is determined from this step on. The coordinate systems S_i, $i = \{1, \ldots, N_h - 1\}$, are used to define surfaces $\Sigma_h^{(i)}$ and $\Sigma_g^{(i)}$ as illustrated in Fig. 14

$$\mathbf{r}_{\mathrm{i}}(u_h, v_h) = \mathbf{M}_{\mathrm{ih}} \mathbf{r}_{\mathrm{h}}(u_h, v_h) \tag{41}$$

$$\mathbf{r}_{\mathrm{i}}(u_g, v_g) = \mathbf{M}_{\mathrm{ih}} \mathbf{r}_{\mathrm{g}}(u_g, v_g) \tag{42}$$

Here,

$$\mathbf{M}_{\mathrm{ih}} = \begin{bmatrix} \cos\left(i \cdot \frac{2\pi}{N_h}\right) & \sin\left(i \cdot \frac{2\pi}{N_h}\right) & 0 & 0 \\ -\sin\left(i \cdot \frac{2\pi}{N_h}\right) & \cos\left(i \cdot \frac{2\pi}{N_h}\right) & 0 & 0 \\ 0 & 0 & 1 & 0 \\ 0 & 0 & 0 & 1 \end{bmatrix} \tag{43}$$

Table 1
Design data of the spherical gear coupling.

Design parameter	[units]	Hub	Sleeve
Tooth number, N_h		13	
Pressure angle, α	deg	30.0	
Module, m	mm	3.0	
Face width, F	mm	30.0	
Generating shift coefficient, χ		-0.058	-0.035
Addendum, h_{ha}	mm	$0.5m$	
Deddendum, h_{hf}	mm	$0.9m$	

Table 2
Design data of the hob.

Design parameter	[units]	Value
Face width, F_w	mm	80.0
Number of threads, N_w		1
Helix hand		Right
Pitch radius, r_w	mm	30.875
Lead angle, λ_w	deg	2.7847
Addendum, h_{wa}	mm	$0.9m$
Deddendum, h_{wf}	mm	$0.5m$
Tip radius, ρ_{edge}	mm	$0.4m$

Step 7 Steps from 1 to 5 are repeated for each pair of tooth surfaces $\Sigma_h^{(i)}$ and $\Sigma_g^{(i)}$, and the angle $\phi_{h,i}$ of rotation of the hub is calculated to obtain a potential contact point for each pair of teeth where there is some clearance. If the deformation of the tooth is sufficient to allow contact, the potential contact point will become a point of contact between the tooth surfaces $\Sigma_h^{(i)}$ and $\Sigma_g^{(i)}$. Likewise, if the potential contact point is outside the boundaries of the tooth surface, it is disregarded.

Step 8 When a pair of tooth surfaces $\Sigma_h^{(i)}$ and $\Sigma_g^{(i)}$ have a potential contact point, the clearance c_i, $i = \{1, \ldots, N_h - 1\}$, is calculated as

$$c_i = \frac{1}{2}(\phi_{h,i} - \phi_h) m N_h \cos\alpha \tag{44}$$

4. Results

The design data of a spherical gear coupling are shown in Table 1. The generating shift coefficients χ set out in Table 1 are determined with a tolerance class $H7/d7$ in accordance with ISO 4156 [27].

These coefficients allow the hub and the sleeve to be generated with a tooth thickness that guarantees the existence of backlash between both splines in the middle cross section. A tool path radius of $r_\beta = 49.0$ mm is assumed to guarantee existence of backlash between both splines along the face width and for a misalignment angle of $\gamma_{\max} = 6.0°$. The design data of the hob to generate the hub are shown in Table 2.

4.1. Geometry comparison

Fig. 15 shows a comparison between the hub tooth surface Σ_h of the proposed model and the tooth surface Σ_{m1} of the simplified model 1, for both tooth sides. A similar comparison between Σ_h and the surface Σ_{m2} of the simplified model 2 is illustrated in Fig. 16. The normal distances from the surface Σ_h to the surfaces Σ_{m1} and Σ_{m2} are used to compare the geometry. These normal deviations are plotted in the radial projection of the hub tooth with axis z_h and the radial position $\rho_i = (x_h^2 + y_h^2)^{1/2}$. The comparisons are limited to the interval $z_h \in [-9.0, +9.0]$ mm, where the maximum deviations reach about 200 m in model 1 and 600 m in model 2. Furthermore, it is important to point out that the Standard ISO 4156 [27] establishes a maximum deviation allowance of the tooth surfaces as 59 m for a standard coupling of $m = 3$ mm, $z = 13$, and tolerance class 7. This means that the obtained deviations between the three models are significant.

The geometry comparison shows that the differences between the compared models arise further away from the middle plane $z_h = 0$. Here, at $z_h = 0$, the three models provide the same cross section.

On the other hand, Fig. 15 shows that the results obtained for the interval $z_h \in [0.0, +9.0]$ mm in the left tooth side (Fig. 15(a)) are exactly the same as those obtained for the interval $z_h \in [-9.0, 0.0]$ mm in the right tooth side (Fig. 15(b)), and *viceversa*. The same observation can be made comparing Fig. 16(a) and 16(b). Since the simplified models do not cause asymmetry in the tooth profiles, this is evidence that the proposed model of generation by a hob is introducing some asymmetry as a consequence of the twist of the tooth surfaces. This phenomenon has been observed in helical gears generated by a hob [28–30], and also in spur gears generated by a hob, although in the latter case it was said to be negligible [31].

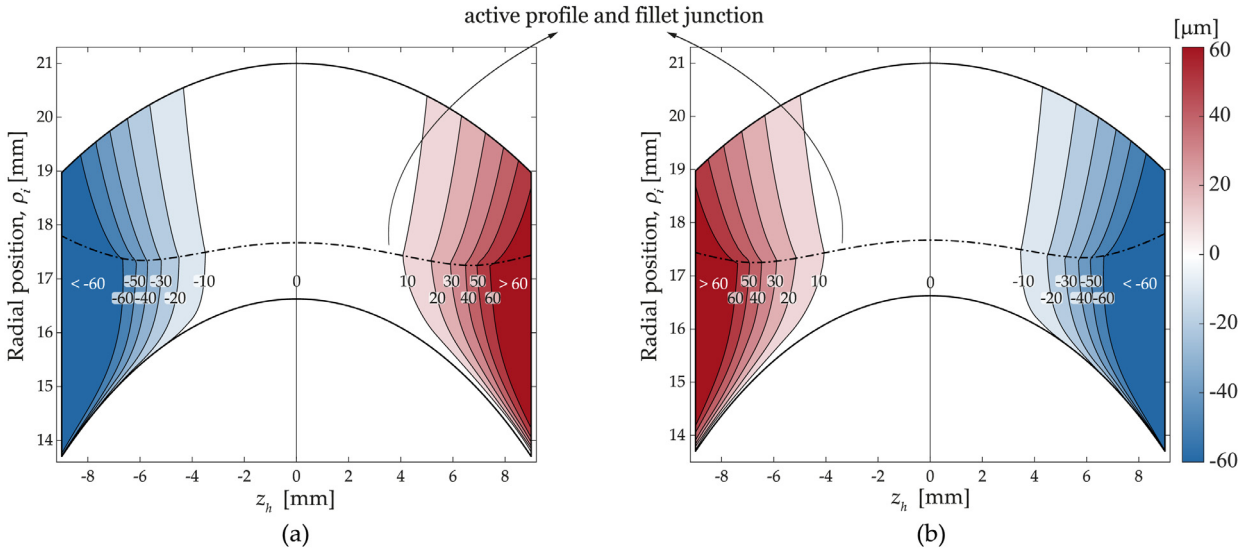

Fig. 15. Normal deviations between Σ_h and Σ_{m1}: (a) left tooth side, and (b) right tooth side.

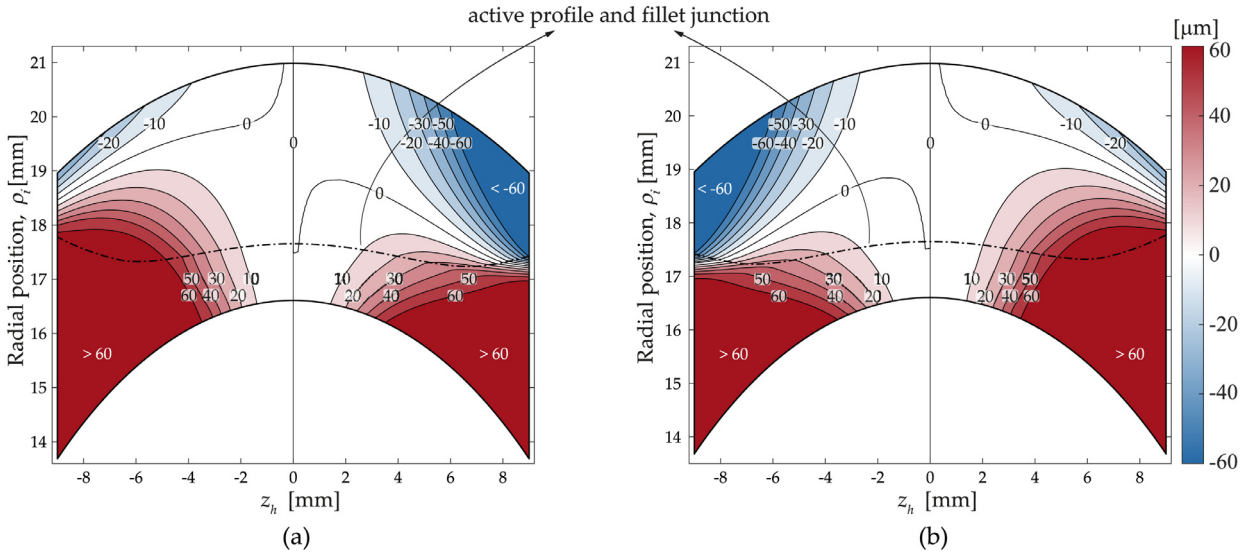

Fig. 16. Normal deviations between Σ_h and Σ_{m2}: (a) left tooth side, and (b) right tooth side.

However, the effect is more notable in spherical gear couplings, as suggested by [12], and may lead to a reduction of the load capacity.

The three models were also compared in terms of the minimum coordinate z_h of the first cross section of the hub tooth where undercutting appears. Fig. 17(a) shows that undercutting emerges at coordinate $z_h = 6.85$ mm in the proposed model, and $z_h = 9.45$ mm in model 2. The location of the cross section where undercutting appears in model 1, $z_h = 7.20$ mm, is very close to that of the proposed model and is not represented in Fig. 17(a) for the purpose of clarity. Fig. 17(b) shows the cross sections of the hub space for the three models at coordinate $z_h = 6.85$ mm, where greater differences can be seen in model 2 than in model 1. It is expected that such differences might have an important effect on the predicted bending strength of the hub, due to the reduction in the tooth thickness. Fig. 17(b) illustrates as well that the tooth profiles of the proposed model are non-symmetric.

In addition, an advantage of the proposed model for hub generation is that it is a procedure focused on the tool path of the hob, in contrast to the other models here compared. Fig. 18(a) shows two possible tool paths: (i) a circular tool path, and (ii) a circular tool path with the influence of the entry and exit of the tool in the hub geometry. Tool entry and exit are relevant to the tooth geometry as stated in AGMA 945-1-B20 [32], especially in those geometries where the teeth are manufactured directly on a shaft and significant reduction of the tooth thickness is undesirable.

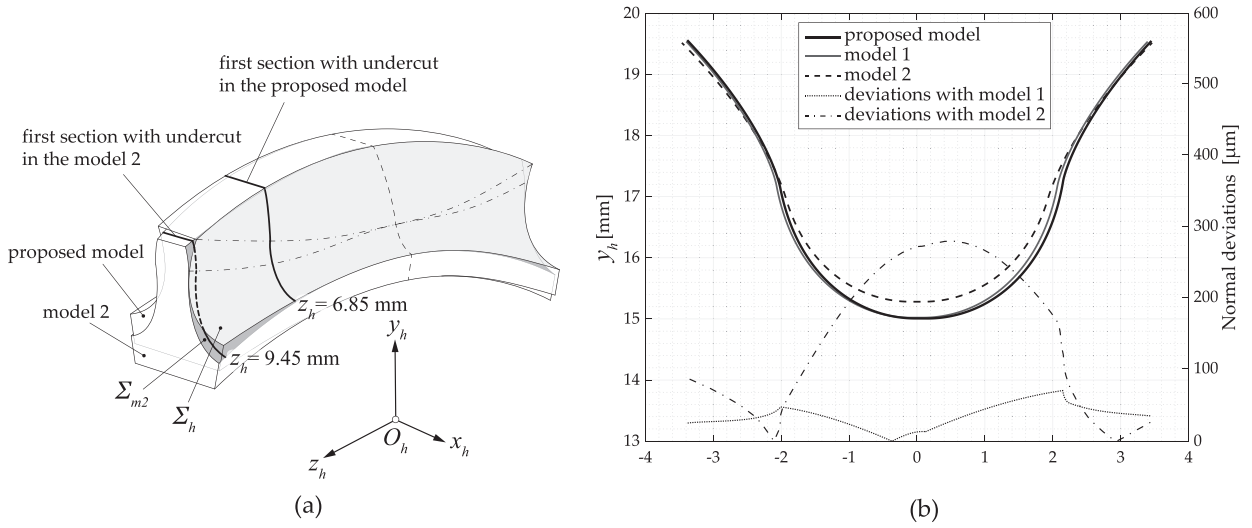

Fig. 17. (a) location of first appearance of undercutting in Σ_h and Σ_{m2}, and (b) hub space cross section comparison at $z_h = 6.85$ mm for Σ_h, Σ_{m1} and Σ_{m2}.

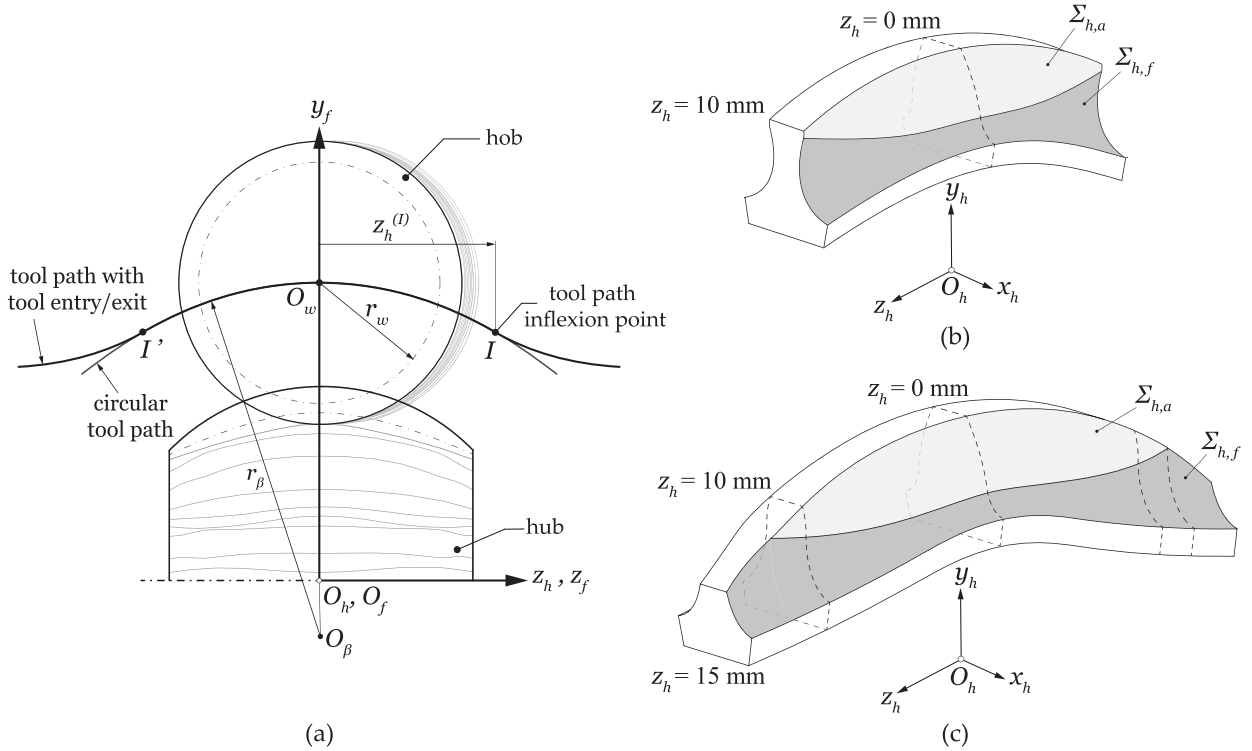

Fig. 18. Tool path entry/exit influence on Σ_h: (a) two types of tool paths, (b) Σ_h using a circular tool path, and (c) Σ_h using a circular tool path with tool entry and exit influence.

Fig. 18 (a) shows that tool entry and exit are controlled through the location of the inflection points I and I', and the curvatures of those tool path sections. Fig. 18(b) illustrates the effect on the hub tooth of a circular path without considering tool entry and exit, and Fig. 18 (c) takes into account its effect. To obtain this geometry with the effect of tool entry and exit, I and I' points are located at $z_h = \pm 15.0$ mm, respectively, and a curvature radii for entry and exit sections equal to the circular tool path radius r_β is used. From both geometries it can be concluded that taking into account the tool entry and exit, a larger face width hub can be generated, preventing the rapid reduction of the tooth thickness, as shown in Fig. 18(b).

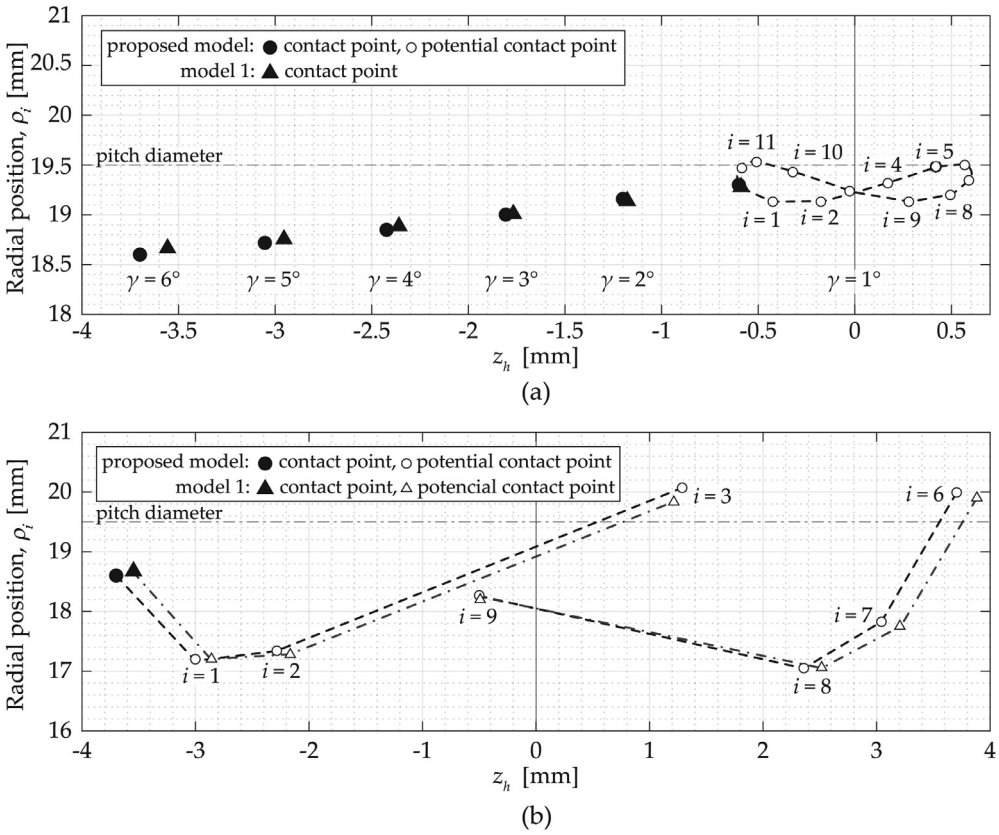

Fig. 19. TCA results: (a) contact points for different values of misalignment angle γ, (b) contact point and potential contact points for $\gamma = 6.0°$.

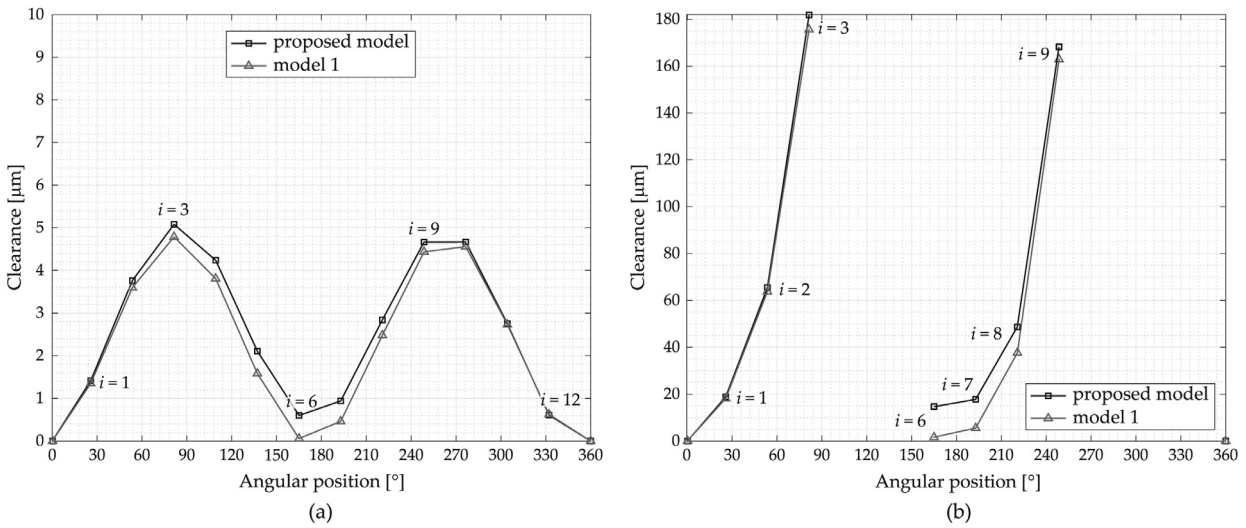

Fig. 20. Clearance values for the potential contact points in case of: (a) $\gamma = 1.0°$, and (b) $\gamma = 6.0°$.

4.2. Unloaded tooth contact and clearance analyses

The results of the tooth contact and clearance analyses of the gear coupling under different values of misalignment γ are illustrated in Figs. 19 and 20. In this section, just the proposed model and model 1 of the hub are being compared, since important geometry differences between the proposed model and model 2 were observed in Section 4.1.

For this analysis, a parabola coefficient $a_p = 0.001$ mm^{-1} (Fig. 3(c)) was used in the generation of the hub to prevent edge contact at the tips of the hub and the sleeve. Fig. 19(a) shows the contact points of the first pair of teeth that comes into contact for misalignment angles $\gamma = \{1^\circ, 2^\circ, 3^\circ, 4^\circ, 5^\circ, 6^\circ\}$. The effect of contact points moving away from the center plane $z_h = 0$ as misalignment increases is in agreement with the literature [12]. The location of the contact points are very similar between the proposed model and model 1 of the hub, although differences increase with the rise of the misalignment angle, up to 144.0 m in coordinate z_h when $\gamma = 6.0^\circ$.

Fig. 19 (a) also depicts the potential contact points for the proposed model of the hub when $\gamma = 1.0^\circ$. Twelve potential contact points are found, numbered from $i = 1$ to $i = 12$ (see also Fig. 14(b)). The locations of the potential contact points for model 1 are very similar to those of the proposed model when $\gamma = 1.0^\circ$, and are not included for clarity. It can also be seen that most of the potential contact points are located below the pitch cylinder of the hub. However, it is expected that the load will cause the contact pattern to be spread over the pitch cylinder [33].

As the misalignment angle increases, not all the tooth pairs have a potential contact point, as those which are out of the hub surface boundaries are disregarded. In case of $\gamma = 6^\circ$, just seven potential contact points are found, in both the proposed model and in model 1 (see Fig. 19(b)).

Clearance distribution is a key parameter to predict load distribution in gear couplings particularly in misaligned conditions, due to its variation along the angular position [2,34,35]. In consequence, Fig. 20 shows clearance distribution at two misalignment angles for those pairs of tooth surfaces $\Sigma_h^{(i)}$ and $\Sigma_g^{(i)}$ that have a potential contact point. It can be observed that clearance is minimum in the pure tilting area (around 0° and 180° of the angular rotation), while it increases in the pure pivoting area (around 90° and 180°), in accordance with the literature. In the case $\gamma = 1.0^\circ$ (Fig. 20(a)), for all the twelve potential contact points found, the clearance distribution and values are very similar for both models of the hub. However, when the misalignment angle is $\gamma = 6.0^\circ$ (Fig. 20(b)), with only seven potential contact points, the differences in the clearance between the proposed model and model 1 are much higher. These deviations may affect load sharing between the teeth of the coupling, as reported in [6,36].

5. Conclusions

This paper presents a procedure to generate an external spherical spline by a hob. This procedure aims to provide a more accurate simulation method for this type of generation process, than methods existing in the scientific literature. To this end, the procedure considers a hob thread surface as a set of cutting edges acting simultaneously during the generation. It makes possible the generation of profiles with undercutting that may appear in the manufacturing of spherical hubs, especially when highly crowned tooth surfaces are required to absorb misalignments above 3°. Moreover, the model presented here can be easily adapted to different tool paths in order to analyze its influence in the generated geometry.

The proposed model for generation of the hub is compared with two existing models in the literature and the following conclusions can be drawn:

(1) The normal deviations between the hub tooth surface of the proposed model and that of the existing models are significant when a high value of crowning is applied to the tooth surface. These differences exceed the maximum deviation allowance established in Standard ISO 4156 [27], especially in the cross sections away from the middle section of the hub.
(2) The prediction of existence of undercutting is closer to the middle cross section according to the proposed model, than that predicted by the existing models. These differences may affect the calculated bending strength of the hub.
(3) The investigation reveals that the proposed model can be easily adapted to follow different tool paths. In this sense, the tool path, which considers the tool entry and exit, is important to obtain larger face widths without thinning the teeth. This will be highly useful in applications where space is limited and the teeth of the hub are directly manufactured on a shaft.
(4) Differences between the proposed model and model 1 of the hub are observed in the location of the contact points and in the clearance values, which may affect contact conditions and thus load distribution. The proposed model predicts slightly larger shifts of the contact points and slightly higher values of clearance than those predicted by the model 1 when misalignment error is present.

The proposed model allows for future work to focus on the optimization of the hub geometry, either through an appropriate tool path of the hob or an appropriate profile crowning of the hub teeth, to balance the clearances, increase the contact ratio and reduce contact and bending stresses of spherical gear couplings.

Declaration of Competing Interest

The authors declare that they have no known competing financial interests or personal relationships that could have appeared to influence the work reported in this paper.

Appendix A. Generation of the sleeve model

Generation of the sleeve tooth surface Σ_g by a shaper requires prior determination of the shaper tooth surface Σ_s. For that purpose, the standard rack-cutter tooth surface Σ_c is defined in Section 2.1 as the generating surface of Σ_s. Finally, the sleeve tooth surface Σ_g is determined.

A1. Generation of the shaper tooth surface Σ_s

Fig. A.21 (a) shows the coordinate systems considered to determine the shaper tooth surface Σ_s. The coordinate systems S_s and S_c are rigidly connected to the shaper and to the rack-cutter, respectively. The system S_n is a fixed coordinate system where the rotation of the shaper is taken into account through the angle ψ_s. The system S_c displaces the value $\psi_s r_s$ in the direction of the axis x_c, which is parallel to the axis x_n. Here, r_s is the pitch radius of the shaper and coincides with the shortest distance between the axes x_c and x_n.

Surface Σ_s can be determined as the envelope to the family of generating tooth surfaces Σ_c in the system S_s by simultaneous consideration of the following equations

$$\mathbf{r}_s(u, v, \psi_s) = \mathbf{M}_{sc}(\psi_s)\mathbf{r}_c(u, v) \tag{A.1}$$

$$f_1(u, v, \psi_s) = \left(\frac{\partial \mathbf{r}_s}{\partial u} \times \frac{\partial \mathbf{r}_s}{\partial v}\right) \cdot \frac{\partial \mathbf{r}_s}{\partial \psi_s} = 0 \tag{A.2}$$

Here,

$$\mathbf{M}_{sc} = \mathbf{M}_{sn}\mathbf{M}_{nc} = \begin{bmatrix} \cos\psi_s & \sin\psi_s & 0 & 0 \\ -\sin\psi_s & \cos\psi_s & 0 & 0 \\ 0 & 0 & 1 & 0 \\ 0 & 0 & 0 & 1 \end{bmatrix} \cdot \begin{bmatrix} 1 & 0 & 0 & -r_s\psi_s \\ 0 & 1 & 0 & r_s \\ 0 & 0 & 1 & 0 \\ 0 & 0 & 0 & 1 \end{bmatrix} \tag{A.3}$$

The shaper teeth are rounded at the tip by considering a tip edge radius. The procedure to define the tip edge of the shaper is similar to the one described for the tip edge of the hob (Section 2.3) and is not described for the purpose of simplicity.

A2. Generation of the sleeve tooth surface Σ_g

Fig. A.21 (b) shows the coordinate systems that are involved in the generation process of the sleeve by a shaper. The system S_f is a fixed coordinate system where rotation of the sleeve is considered. Similarly, system S_n is an auxiliary fixed

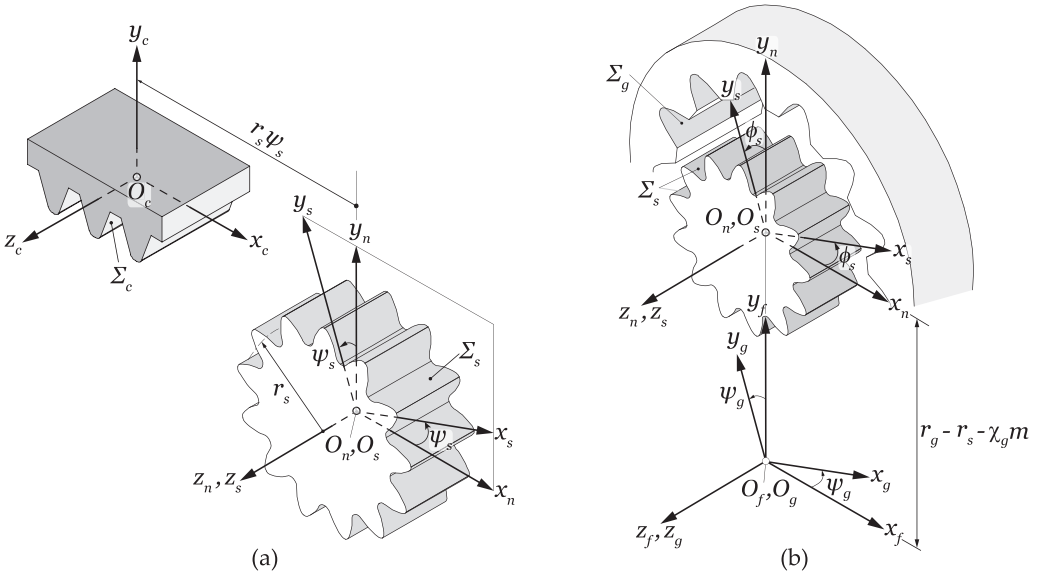

Fig. A.21. Definition of the sleeve model: (a) generation of the shaper tooth surface Σ_s, and (b) generation of the sleeve tooth surface Σ_g.

coordinate system where rotation of the shaper occurs. The system S_s, rigidly connected to the shaper, rotates the angle ϕ_s while the system S_g, rigidly connected to the sleeve, rotates the angle ψ_g, which is given as

$$\psi_g = \phi_s \frac{N_s}{N_h} \tag{A.4}$$

where N_h is the number of teeth of the hub (which is equal to that of the sleeve in a gear coupling) and N_s is the number of teeth in the shaper.

The surface Σ_g is determined as the envelope to the family of surfaces Σ_s in coordinate system S_g by simultaneous consideration of the following equations

$$\mathbf{r}_g(u, v, \psi_s, \phi_s) = \mathbf{M}_{gs}(\phi_s)\mathbf{r}_s(u, v, \psi_s) \tag{A.5}$$

$$f_1(u, v, \psi_s) = \left(\frac{\partial \mathbf{r}_s}{\partial u} \times \frac{\partial \mathbf{r}_s}{\partial v}\right) \cdot \frac{\partial \mathbf{r}_s}{\partial \psi_s} = 0 \tag{A.6}$$

$$f_2(u, v, \psi_s, \phi_s) = \left(\frac{\partial \mathbf{r}_g}{\partial u} \times \frac{\partial \mathbf{r}_g}{\partial v}\right) \cdot \frac{\partial \mathbf{r}_g}{\partial \phi_s} = 0 \tag{A.7}$$

Here, $\mathbf{M}_{gs}$ is the matrix for coordinate transformation from the system S_s to the system S_g

$$\mathbf{M}_{gs} = \mathbf{M}_{gf}\mathbf{M}_{fn}\mathbf{M}_{ns} \tag{A.8}$$

$$\mathbf{M}_{gs} = \begin{bmatrix} \cos\psi_g & \sin\psi_g & 0 & 0 \\ -\sin\psi_g & \cos\psi_g & 0 & 0 \\ 0 & 0 & 1 & 0 \\ 0 & 0 & 0 & 1 \end{bmatrix} \cdot \begin{bmatrix} 1 & 0 & 0 & 0 \\ 0 & 1 & 0 & r_g - r_s - \chi_g m \\ 0 & 0 & 1 & 0 \\ 0 & 0 & 0 & 1 \end{bmatrix} \cdot \begin{bmatrix} \cos\phi_s & -\sin\phi_s & 0 & 0 \\ \sin\phi_s & \cos\phi_s & 0 & 0 \\ 0 & 0 & 1 & 0 \\ 0 & 0 & 0 & 1 \end{bmatrix} \tag{A.9}$$

where r_g is the pitch radius of the sleeve and χ_g is a generating shift coefficient. A negative value of χ_g may be applied to produce some backlash between the hub and the sleeve teeth.

References

[1] S. Hahn, Coupling Connections and Splines, in: Encyclopedia of Automotive Engineering, American Cancer Society, 2014, pp. 1–14, doi:10.1002/9781118354179.auto094.
[2] M. Alfares, A. Falah, A. Elkholy, Clearance distribution of misaligned gear coupling teeth considering crowning and geometry variations, Mech Mach Theory 41 (10) (2006) 1258–1272, doi:10.1016/j.mechmachtheory.2005.11.004.
[3] Y. Guan, X. Yang, Z. Fang, G. Chen, Comparative analysis of three geometric models for crown gear coupling, Mech Mach Theory 136 (2019) 269–283, doi:10.1016/j.mechmachtheory.2019.02.016.
[4] R. Baker, Durability of Steel Spline Couplings, Ph.D. thesis, University of London, 2005.
[5] V. Cuffaro, F. Curà, A. Mura, Test rig for spline couplings working in misaligned conditions, J Tribol 136 (1) (2014) 011104, doi:10.1115/1.4025656.
[6] J. Hong, D. Talbot, A. Kahraman, Load distribution analysis of clearance-fit spline joints using finite elements, Mech Mach Theory 74 (2014) 42–57, doi:10.1016/j.mechmachtheory.2013.11.007.
[7] Y. Guo, S. Lambert, R. Wallen, R. Errichello, J. Keller, Theoretical and experimental study on gear-coupling contact and loads considering misalignment, torque and friction influences, Mech Mach Theory 98 (2016) 242–262, doi:10.1016/j.mechmachtheory.2015.11.015.
[8] J.R. Mancuso, Couplings and joints: design, selection and application, Technology & Engineering (1986). M. Dekker
[9] W. Herbstritt, J. Paluh, Mill spindle advanced gear design, Iron and Steel Engineers 76 (7) (1999) 44–48.
[10] P. Krot, Transient Torsional Vibrations Control in the Geared Drive Trains of the Hot Rolling Mills, in: IEEE International Conference on Control Applications, St. Petersburg, 2009, pp. 1368–1373, doi:10.1109/CCA.2009.5280933.
[11] J. Larrañaga, A. Arana, I. Ulacia, J. Esnaola, I. Torca, Misalignment Effect on Contact Pressure and Tooth Root Strength of Spline Couplings, in: 5th International Conference on Power Transmission-BAPT, Ohrid, Macedonia, 2016.
[12] F. Ohshima, S. Hirata, H. Yoshino, Study on tooth contact of gear couplings, Transactions of the Japan society of mechanical engineers. Series C 78 (786) (2012) 639–649.
[13] K. Mitome, T. Okuda, T. Ohmachi, T. Yamazaki, Development of a new hobbing of spherical gear, Transactions of the Japan society of mechanical engineers. Series C 66 (646) (2000) 1975–1980.
[14] L. Chao, C. Tsay, Contact characteristics of spherical gears, Mech Mach Theory 43 (10) (2008) 1317–1331, doi:10.1016/j.mechmachtheory.2007.10.008.
[15] L. Kelemen, J. Szente, Two mathematical models for generation of crowned tooth surface, The Scientific World Journal (2014), doi:10.1155/2014/641091.
[16] F. Litvin, Theory of Gearing, Tech. rep., University of Illinois at Chicago, 1989.
[17] F. Litvin, A. Fuentes, Gear Geometry and Applied Theory, 2nd Edition, CAMBRIDGE University Press, 2004.
[18] F. Litvin, A. Fuentes, C. Zanzi, M. Pontiggia, Design, generation, and stress analysis of two versions of geometry of face-gear drives, Mech Mach Theory 37 (10) (2002) 1179–1211, doi:10.1016/S0094-114X(02)00050-2.
[19] F. Litvin, D. Vecchiato, E. Gurovich, A. Fuentes, I. Gonzalez-Perez, K. Hayasaka, K. Yukishima, Computerized developments in design, generation, simulation of meshing, and stress analysis of gear drives, Meccanica 40 (2005) 291–324, doi:10.1007/s11012-005-4020-y.
[20] F. Litvin, I. Gonzalez-Perez, K. Yukishima, A. Fuentes, K. Hayasaka, Generation of planar and helical elliptical gears by application of rack-cutter, hob, and shaper, Comput Methods Appl Mech Eng 196 (41–44) (2007) 4321–4336, doi:10.1016/j.cma.2007.05.003.
[21] F. Litvin, A. Fuentes, I. Gonzalez-Perez, K. Hayasaka, Noncircular gears: Design and generation, CAMBRIDGE University Press, 2009.
[22] Y. Wu, W. Hsu, A general mathematical model for continuous generating machining of screw rotors with worm-shaped tools, Appl Math Model 38 (1) (2014) 28–37, doi:10.1016/j.apm.2013.05.056.
[23] K. Jia, J. Guo, S. Zheng, J. Hong, A general mathematical model for two-parameter generating machining of involute cylindrical gears, Appl Math Model 75 (2019) 37–51, doi:10.1016/j.apm.2019.05.021.
[24] L. Vedmar, A parametric analysis of the gear surface roughness after hobbing, J. Mech. Des. 132 (11) (2010) 111004, doi:10.1115/1.4002655.

[25] F. Klocke, C. Brecher, C. Lopenhaus, M. Kromer, Calculating the workpiece quality using a hobbing simulation, Procedia CIRP 41 (2016) 687–691, doi:10.1016/j.procir.2015.12.045.
[26] I. Ulacia, J. Larrañaga, A. Arana, A. Iñurritegui, J. Elizegi, Fatigue Life Prediction of Spherical Gear Couplings, in: American Gear Manufacturers Association Fall Technical Meeting 2018, Illinois, 2018, pp. 202–207.
[27] I.O.f. Standardization, ISO 4156: Straight cylindrical involute splines, 2005.
[28] J. Lange, How Are You Dealing with the Bias Error in Your Helical Gears? in: American Gear Manufacturers Association Fall Technical Meeting, 2008, pp. 227–240.
[29] O. Winkel, New Developments in Gear Hobbing, in: American Gear Manufacturers Association Fall Technical Meeting, 2009, pp. 43–60.
[30] V. Tran, R. Hsu, C. Tsay, Study on the anti-twist helical gear tooth flank with longitudinal tooth crowning, J. Mech. Des. 136 (6) (2014) 061007, doi:10.1115/1.4027166.
[31] LMT-Fette-Inc., Finish hobbing crowned helical gears without twist, Gear Technology February (2006) 12–13.
[32] American Gear Manufacturers Association, AGMA 945-1-b20: Splines design and application, 2020.
[33] R. Cedoz, M. Chaplin, Design guide for involute splines, Society of Automotive Engineers (1994).
[34] K. Nakashima, Teeth contact behaviour and load distribution of gear couplings, Trans. Jpn. Soc. Mech. Eng. 502 (Part C 54) (1988) 1302–1307, doi:10.1299/kikaic.54.1302.
[35] R. Beckmann, Beitrag Zur Auslegung Und Konstruktion Von Balligzahn-kupplungen, Ph.D. thesis, Chemmitz Technology University, 2005.
[36] F. Curà, A. Mura, Experimental and theoretical investigation about reaction moments in misaligned splined couplings, Mech Syst Signal Process 45 (2) (2014) 504–512, doi:10.1016/j.ymssp.2013.12.005.